Reconciling different approaches to quantifying land surface temperature impacts of afforestation using satellite observations

Huanhuan Wang[1], Chao Yue[2,3*], Sebastiaan Luyssaert[4]

[1]College of Natural Resources and Environment, Northwest A&F University, Yangling, Shaanxi 712100, P. R. China

[2] State Key Laboratory of Soil Erosion and Dryland Farming on the Loess Plateau, Northwest A&F University, Yangling, Shaanxi 712100, P. R. China

[3] College of Forestry, Northwest A&F University, Yangling, Shaanxi 712100, P. R. China

[4] Department of Ecological Sciences, Faculty of Sciences, Vrije Universiteit Amsterdam, Amsterdam 1081 HV, The Netherlands

Correspondence: Chao Yue, State Key Laboratory of Soil Erosion and Dryland Farming on the Loess Plateau, Northwest A&F University, Yangling, Shaanxi 712100, P. R. China

E-mail: chaoyue@ms.iswc.ac.cn

Abstract

Satellite observations have been widely used to examine afforestation effects on local surface temperature at large spatial scales. Different approaches, which potentially lead to differing definitions of the afforestation effect, have been used in previous studies. Despite their large differences, the results of these studies have been used in climate model validation and cited in climate synthesis reports. Such differences have been simply treated as observational uncertainty, which can be an order of magnitude bigger than the signal itself. Although the fraction of the satellite pixel actually afforested has been noted to influence the magnitude of afforestation effect, it remains unknown whether it is a key factor which can reconcile the different approaches. Here, we provide a synthesis of three influential approaches (one

estimates the actual effect and the other two the potential effect) and use large-scale afforestation over China as a test case to examine whether the different approaches can be reconciled. We found that the actual effect (ΔT_a) often relates to incomplete afforestation over a medium resolution satellite pixel (1km). ΔT_a increased with the afforestation fraction, which explained 89% of its variation. One potential effect approach quantifies the impact of quasi-full afforestation (ΔT_{p1}), whereas the other quantifies the potential impact of full afforestation (ΔT_{p2}) by assuming a shift from 100% openland to 100% forest coverage. An initial paired-samples *t*-test shows that $\Delta T_a < \Delta T_{p1} < \Delta T_{p2}$ for the cooling effect of afforestation ranging from 0.07K to 1.16K. But when all three methods are normalized for full afforestation, the observed range in surface cooling becomes much smaller (0.79K to 1.16K). Potential cooling effects have a value in academic studies where they can be used to establish an envelope of effects, but their realization at large scales is challenging given its nature of scale dependency. The reconciliation of the different approaches demonstrated in this study highlights the fact that the afforestation fraction should be accounted for in order to bridge different estimates of surface cooling effects in policy evaluation.

Keywords: surface temperature change, afforestation, actual effect, potential effect, reconciliation, surface energy balance, China

1 Introduction

Afforestation has been and is still proposed as an effective strategy to mitigate climate change because forest ecosystems are able to sequester large amounts of carbon in their biomass and soil, slowing the increase of atmospheric CO_2 concentration (Fang et al., 2014; Pan et al., 2011). Additionally, forests regulate the exchange of energy and water between the land surface and

the lower atmosphere through various biophysical effects, including radiative processes such as surface reflectance, and non-radiative processes such as evapotranspiration and sensible heat flux (Bonan, 2008; Juang et al., 2007). As the net result of the surface energy balance, land surface temperature (LST) is widely used to measure the local climatic impact of afforestation (Li et al., 2015; Winckler et al., 2019a).

Climate model simulations and site-level observations have been utilized to explore the impact of forest dynamics on land surface temperature (Lee et al., 2011; Pitman et al., 2009; Swann et al., 2012). However, afforestation impacts on local LST derived from models tend to be highly uncertain as they are limited by the coarse spatial resolution of models and uncertainties in model parameters and processes (Oleson et al., 2013; Pitman et al., 2011), while insights from site-level assessments cannot be extrapolated to large spatial domains (Lee et al., 2011). Alternatively, remote sensing-based LST products enable the assessment of local LST changes due to forest dynamics on large spatial scales (Li et al., 2015; Shen et al., 2020).

A number of studies investigated the surface temperature impact of afforestation based on satellite observations and they have been cited in high-level climate science synthesis reports (e.g., *IPCC Special Report on Climate and Land* authored by Jia et al., 2019), even though there are large differences in afforestation impacts on LST between different methods. For example, Alkama and Cescatti (2016), found a cooling effect of about 0.02K from afforestation in temperate regions, while Li et al. (2015) reported a 0.27±0.03K 'potential' cooling from afforestation in the northern temperate zone (20–50° N) based on the 'space-for-time' method. In contrast, Duveiller et al. (2018) found a much stronger 'potential' cooling effect of 2.75K for afforestation in the northern temperate region. While such differences were acknowledged in a recent modelling study (Winckler et al., 2019b), they were simply treated as observational

76   uncertainty for climate model evaluation, with the uncertainty range being as big as, or even an

77   order of magnitude larger than, the afforestation effect. It remains unclear whether the

78   differences arising from these different methods can be reconciled.

79

80   Until now, studies using satellite data to investigate afforestation impact on surface temperature

81   have mainly focused on three methods. The first method, termed the 'space-and-time' approach

82   (Fig. 1, red box), aims to examine the actual, realized effect of afforestation ('actual effect') by

83   isolating the forest cover change effect from the gross temperature change over time in places

84   where forest cover change actually occurred (Alkama and Cescatti, 2016; Li et al., 2016a). The

85   second method, termed the 'space-for-time' approach (Fig. 1, orange box), compares the

86   surface temperature of forest with adjacent 'openland' (i.e., cropland or grassland) under similar

87   environmental conditions (e.g., background climate and topography) and estimates the

88   'potential effect' of afforestation if afforestation were to occur (Ge et al., 2019; Li et al., 2015;

89   Peng et al., 2014). Note that such effects are often quantified using medium-resolution land-

90   cover datasets (typical resolution = 1km), which do not necessarily represent 100% ground

91   coverage, and we therefore term such a potential effect a 'mixed potential effect'.

92

93   The third method, recently used by Duveiller et al. (2018), uses the 'singular value

94   decomposition' technique (Fig. 1 green box), which is claimed to extract the hypothetical LST

95   for different land-cover types by assuming a 100% coverage of the target cover type. The

96   afforestation effect on LST is then quantified as the difference between the LST of a pixel with

97   a hypothetical 100% forest coverage and the LST of an adjacent pixel with 100% openland

98   coverage. As with the second method, such an approach quantifies the 'potential effect' of

99   afforestation, but in this case, it quantifies the 'full potential effect' by assuming transitions

100   between land-cover types with 100% complete ground coverage.

101   Previous studies have revealed the fraction of forest change as an important factor determining

102   the magnitude of the afforestation effect. Alkama and Cescatti (2016) indicated that the actual

103   temperature effect is fraction-dependent, and Li et al. (2016a) pointed out that use of a higher

104   threshold to define forest change resulted in a stronger potential effect. Nonetheless, whether

105   the fraction of forest change can explain the differences in the afforestation effect produced by

106   different methods, e.g., whether the 'potential' effect can be 'actualized', has not been

107   demonstrated. Testing the role of afforestation fraction in reconciling the afforestation effects

108   produced by different methods can help clarify potential confusion and contribute to appropriate

109   policy evaluation.

110

111   This study develops detailed conceptual and methodological descriptions for each of the three

112   approaches and uses large-scale afforestation over China as a case study to compare the three

113   approaches. We tested the following hypotheses: (1) The actual effect on LST increases with

114   the area that has actually been afforested, defined as afforestation intensity (or F_{aff}). (2) The

115   actual effect is smaller than the potential effects. (3) When extending F_{aff} to a hypothetical value

116   of 100%, the actual effect approaches the potential effect. If proven, this third hypothesis

117   implies that the LST impacts from different approaches could be reconciled given the same

118   boundary condition of full afforestation. In that case, we then have a fourth hypothesis (4)

119   stating that changes in underlying biophysical processes including radiation, sensible and latent

120   heat fluxes that drive LST changes should also be reconciled among different methods. To keep

121   the focus on reconciling methodological differences, only changes in the daytime surface

122   temperature were considered in this study. Nevertheless, similar conclusions regarding the

123   different approaches are expected for nighttime surface temperature.

124

125
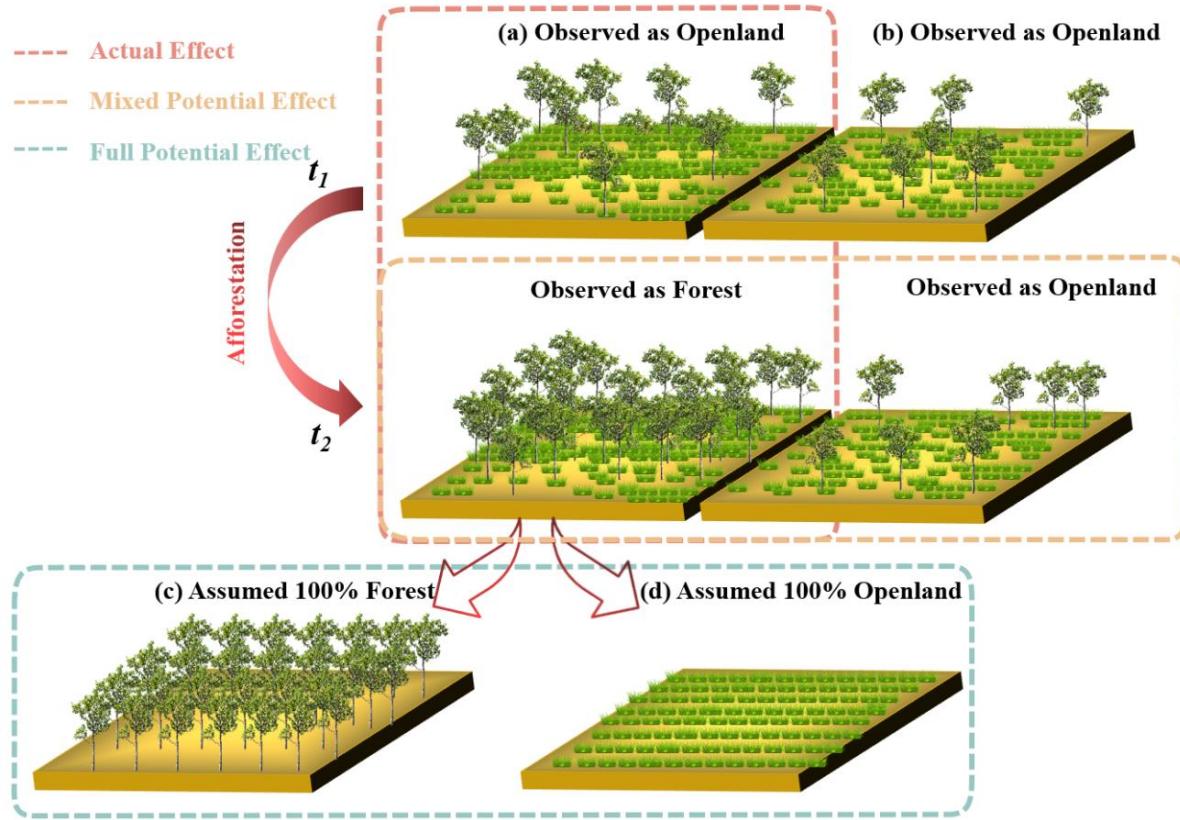
Figure 1. Illustration of the three approaches to quantifying the local surface temperature effect of afforestation. (a) and (b) represent two nearby pixels, both classified as openland at time t_1 by medium-resolution satellites (1km spatial resolution), with one of them classified as forest at time t_2 (i.e., having experienced afforestation) and the other unchanged. Note, neither of these pixels will have 100% complete coverage of either openland (i.e., grassland or cropland) or forest, but they will have been classified as either openland or forest by medium-resolution satellite products. (c) and (d) represent pixels with 100% forest or 100% openland coverage whose temperature can be derived from pixels of mixed land cover types by using the singular value decomposition (SVD) technique (Duveiller et al., 2018). The red dotted box describes the quantification of the 'actual effect' of afforestation (ΔT_a) occurring from t_1 to t_2 by the 'space-and-time' method. The orange box represents the 'mixed potential effect' determined by hypothesizing potential shifts between openland and forest based on the 'space-for-time' approach (ΔT_{p1}). The green box represents the 'full potential effect' of afforestation (ΔT_{p2})

139   derived by hypothesizing a transition from 100% complete openland coverage to 100%

140   complete forest coverage.

141

2 Methods

143   2.1 Three Approaches to Quantifying the Impacts of Afforestation on LST

144
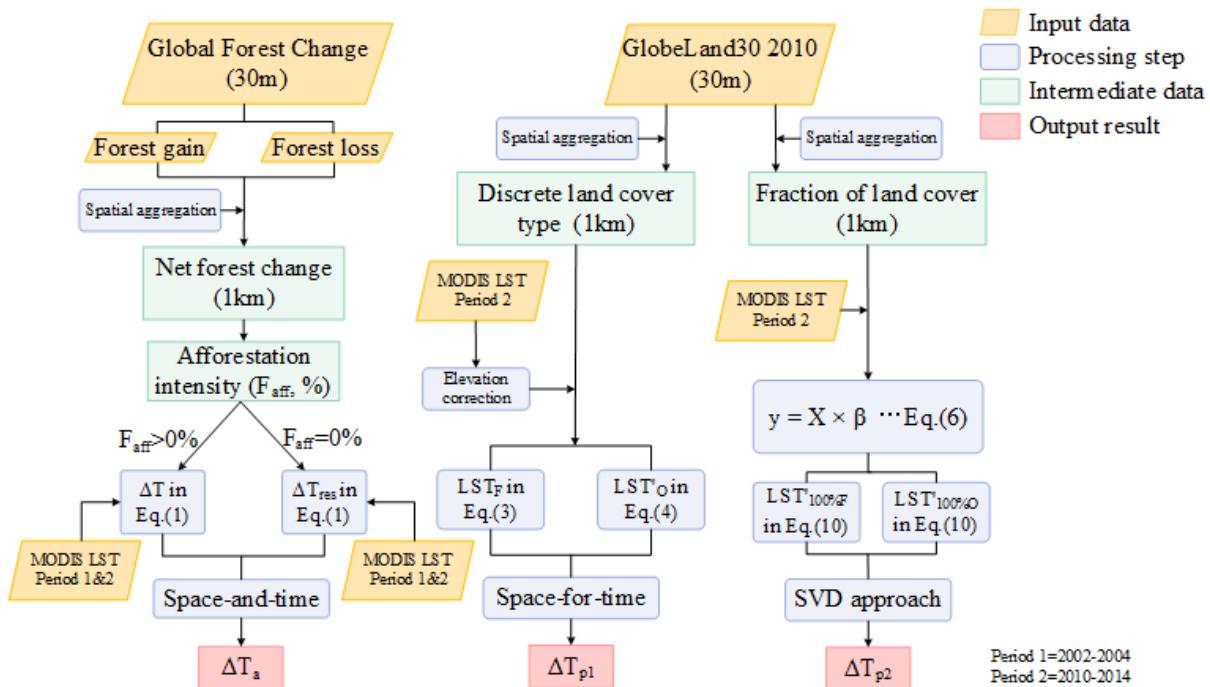
Figure 2. Schematic overview of the processing steps. The different output results correspond

146   to actual effect (ΔT_a), mixed potential effect (ΔT_{p1}) and full potential effect of afforestation

147   (ΔT_{p2}).

148

149   2.1.1 Actual Effect of Afforestation (ΔT_a)

150

151   The 'space-and-time' approach assumes that the gross change in land surface temperature (ΔT)

152   over a given time period during which afforestation occurred, contains both signals of

153   temperature change due to afforestation (ΔT_a) and background temperature variation (ΔT_{res})

154   due to changes in large-scale circulation patterns (Alkama and Cescatti, 2016; Li et al., 2016a):

155 $$\Delta T = \Delta T_a + \Delta T_{res} \tag{1}$$

156 where ΔT is the gross temperature change during the period from t_1 to t_2 for the pixel under

157 study. ΔT can be calculated as the difference between LST_{t2} and LST_{t1}, with LST_{t2} being the

158 surface temperature after afforestation and LST_{t1} being that before afforestation. It thus follows

159 that

160 $$\Delta T_a = \Delta T - \Delta T_{res} \tag{2}$$

161 ΔT_{res} can be approximated by averaging changes in surface temperature for those pixels

162 adjacent to the target afforestation pixel for which the forest cover remained constant between

163 t_1 and t_2 (i.e., $F_{aff} = 0\%$; section 2.2.2). Here, pixels with $F_{aff} > 0\%$ were defined as afforestation

164 target pixels. A searching window of 11 km by 11 km was established, centered on the

165 afforestation pixel. Within this window, pixels with $F_{aff} = 0\%$ were defined as control pixels and

166 were used to derive ΔT_{res}. Afforestation pixels and adjacent control pixels were both determined

167 based on the net forest change between t_1 and t_2 using Global Forest Change (GFC) data (Fig.

168 2; Section 2.2.2).

169

170 2.1.2 Mixed Potential Effect (ΔT_{p1})

171

172 The 'space-for-time' method relies on the 'space-substitute-for-time' assumption to obtain the

173 potential impact of afforestation on local temperature (Zhao and Jackson, 2014). By assuming

174 that forest and openland share the same environmental conditions (background climate,

175 topography, etc.) within a small spatial domain, the potential temperature effect of afforestation

176 is examined using the search window method with a window size of up to 40km×40km (Ge et

177 al., 2019; Li et al., 2015; Peng et al., 2014). Here, to be consistent with our 'actual effect'

178 approach, a more conservative window size of 11km×11km was used, smaller than that used in

179 the majority of previous studies (Ge et al., 2019; Li et al., 2015; Peng et al., 2014). In most

180   previous studies, existing medium resolution (1km) land-cover maps were used directly. Such

181   land-cover products rely on certain thresholds to classify satellite pixels into discrete land-cover

182   types. Given the widespread spatial heterogeneity in land-cover distribution, it is to be expected

183   that only in rare cases will these medium-resolution pixels have 100% coverage of a given land-

184   cover type. Therefore, when determined in this way, the potential effect of afforestation has

185   been named the 'mixed potential effect', in contrast to the 'full potential effect', on which we

186   will focus in the next section, which assumes a potential transition between land-cover types of

187   100% coverage.

188

189   To ensure consistency with the land-cover data used in the 'full potential effect' approach (i.e.,

190   the SVD method), the GlobeLand30 land-cover map was aggregated from its original resolution

191   (30m) to 1km resolution. The land-cover type assigned to a given 1km pixel during aggregation

192   was based on the land-cover type with an area fraction >50% within that pixel, to be consistent

193   with the rationale behind the generation of medium-resolution land-cover products (Section

194   2.2.2). A 1km forest pixel was then chosen as the target pixel and put at the center of a search

195   window with dimensions 11km×11km. The 'mixed potential effect' of afforestation (ΔT_{p1}) was

196   defined as the difference between the temperature of the target pixel (LST_F) and the average

197   temperature of all the surrounding openland pixels within the window ($\overline{LST_O^{'}}$):

198                                    $$\Delta T_{p1} = LST_F - \overline{LST_O^{'}}\qquad\qquad(3)$$

199   where LST_F is the surface temperature of the target forest pixel at t_2, and $LST_O^{'}$ represents the

200   elevation-corrected surface temperature of openland pixels at t_2 within the search window.

201   Given our search window size, ΔT_{p1} could be biased by the elevation difference between the

202   target forest pixel and surrounding openland pixels. Therefore, a linear relationship was first

203   fitted between the observed openland temperature, LST_O, and the elevation of the openland

204   pixel (Ele_O). This fitted temperature lapse rate was then used to derive elevation-corrected

205   openland temperature $LST_O^{'}$:

$$LST_O^{'} = LST_O + k \times \Delta Ele_{F-O} \tag{4}$$

207   where ΔEle_{F-O} is the elevation difference between forest and openland pixels. The elevation is

208   available   from   NASA's   Shuttle   Radar   Topography   Mission   (SRTM)   data

209   (https://lpdaac.usgs.gov/products/srtmgl1v003/).

210

211   2.1.3 Full Potential Effect (ΔT_{p2})

212

213   The full potential effect represents the temperature change due to hypothesizing a shift from

214   100% openland to 100% forest coverage, and was determined here by employing the singular

215   value decomposition (SVD) method used in Duveiller et al. (2018). The SVD technique

216   assumes that the temperature observed for a pixel at 1km scale is a linear composition of the

217   temperatures of different land-cover types at a finer resolution (in our study at a 30m resolution).

218   For each 1km pixel, the observed temperature can be written as the composition of the

219   temperature of each component land-cover type and its corresponding fraction, based on the

220   land-cover fractions derived from the 30m-resolution GlobeLand30 map (Section 2.2). The

221   temperature of each type of land cover was assumed constant within a search window of 11km

222    $\times$ 11km. For each given search window, the following equations can be obtained:

$$\begin{pmatrix} y_1 \\ \vdots \\ y_n \end{pmatrix} = \begin{pmatrix} x_{11} & \cdots & x_{1m} \\ \vdots & \ddots & \vdots \\ x_{n1} & \cdots & x_{nm} \end{pmatrix} \times \begin{pmatrix} \beta_1 \\ \vdots \\ \beta_m \end{pmatrix} \tag{5}$$

224   where n is the total number of 1km pixels within the window, after accounting for the elevation

225   difference (thus the maximum value of n is 121 given our 11km $\times$ 11km search window), m is

226   the number of land-cover types, x_{ij} refers to the fraction of land-cover type j in pixel i, β_i refers

227   to the temperature of land cover type i. To minimize elevation impacts, the linear regression

228   relationship for a given 1km pixel was included only when the elevation difference between

229   this pixel and the central pixel of the search window was smaller than 100m. Using matrix

230   notation, Eq. (5) can be simplified to:

231                                    $$y = X \times \beta \qquad (6)$$

232   where the matrix X contains land-cover fraction for the n 1km pixels as an explanatory variable,

233   the response variable y contains n LST observations, and the coefficient vector, β, contains the

234   regression coefficients which show temperatures of different land-cover types. Note that this

235   linear equation system cannot be easily solved because the matrix X is 'closed', i.e., by

236   definition, the elements in each row of the matrix X add to 1. After removing the mean of each

237   column (Zhang et al., 2007), the matrix X was transformed, by applying the SVD technique, to

238   another matrix, Z, of reduced dimension (more details in Duveiller et al., 2018). After this

239   transformation, we have the following:

240                                    $$y = Z \times \beta^{'} + \varepsilon \qquad (7)$$

241   in which the β' coefficient can be obtained from equation (8):

242                                    $$\beta^{'} = \left(Z^{t}Z \right)^{-1} Z^{t}y \qquad (8)$$

243   However, the β' vector calculated from the transformed matrix Z cannot directly provide

244   surface temperatures for corresponding land-cover types. To obtain temperatures for each land-

245   cover type by assuming 100% ground coverage, an identity matrix Y with its dimension equal

246   to the number of land-cover types must be constructed to represent the hypothetical case in

247   which each 1km pixel was 100% covered by a single land-cover type. The same transformation

248   as applied to the matrix X was then applied to Y, to obtain a transformed matrix Z'. Finally, the

249   predicted temperature ($LST_{100\%}^{'}$) for each land-cover type assuming a 100% coverage is

250   calculated as:

251 $$LST'_{100\%} = Z' \beta' \qquad (9)$$

252 For the central pixel of the local search window, ΔT_{p2} is defined as the difference between the

253 predicted $LST'_{100\%}$ for forest ($LST'_{100\%F}$) and openland ($LST'_{100\%O}$).

254 $$\Delta T_{p2} = LST'_{100\%F} - LST'_{100\%O} \qquad (10)$$

255 More details, including an illustration of the SVD method, can be found in Fig. 7 in Duveiller

256 et al. (2018).

257

258 At the scale of the searching windows used in this analysis (11km×11km), any nonlocal effects

259 cancel out when comparing temperature differences over neighboring areas because the effects

260 of advection and atmospheric circulation have been reported to be similar for adjacent areas

261 (Pongratz et al., 2021; Winckler et al., 2019a). Hence the quantified afforestation effect for each

262 of the three methods can be considered to be the local effect only.

263

264 ## 2.2 Dataset and Processing

265 2.2.1 The Test Case: Large-scale Afforestation over China

266

267 China was selected as the test case for addressing the important methodological issues in

268 quantifying land surface impacts of afforestation because afforestation is a key national strategy

269 for sustainable development and climate mitigation (Bryan et al., 2018; Qi et al., 2013).

270 According to the 8th National Forest Inventory conducted in 2013, China's afforestation area

271 has reached 6.9×10^3 million ha, accounting for 33% of the total global afforestation area (Chen

272 et al., 2019). Afforestation in China during 2000–2012 occurred mainly in regions with more

273 than 400 mm of precipitation per year (Fig. 3a), which is considered a threshold below which

274 there is a high risk of afforestation failing due to water limitation (Mátyás et al., 2013). China

275 covers a wide range of latitude from 3.9° N to 53.6° N and its forest ecosystems cover an

276 elevation range of 100m to 4000m. This wide range of climate zones, from tropical/subtropical

277 to temperate and boreal, make it highly suitable for our methodological analysis because the

278 impact of afforestation on LST might differ with latitude and background climate (Lee et al.,

279 2011; Alkama and Cescatti, 2016). Further justification for using China as a test case comes

280 from the strongly diverging published LST impacts of afforestation there, which range from an

281 actual effect of -0.0036K decade^{-1} by Li et al. (2020) to a potential effect of -1.1K by Peng et

282 al. (2014).

283

284 2.2.2 MODIS Dataset and Preparation

285

286 In this study, the actual effect was estimated by combining the actual satellite-derived

287 afforestation for 2000 to 2012 (see Section 2.2.2) with satellite-based estimates of biophysical

288 variables for the periods 2002–2004 (t_1) and 2010–2014 (t_2). MODIS remote sensing products

289 for land surface temperature (MOD11A2), albedo (MCD43B3) and evapotranspiration

290 (MOD16A2) were used to characterize the biophysical effects (Table 1). The datasets were

291 regridded to harmonize with spatial (1km) and temporal (annual) resolutions (Table 1).

292

293 The MOD11A2 product provides 8-day land surface temperature for 10:30 AM and 22:30 PM

294 from the Terra satellite, but here we focused on daytime surface temperature. Only valid LST

295 observations from the original data were used to compute the average daily values for a given

296 year. Years for which more than 40% of daily data are missing were excluded from the analysis.

297 Annual data were then aggregated to obtain the average annual temperature for periods t_1 and

298 t_2.

299

300   The MCD43B3 product provides white-sky and black-sky shortwave albedo at 16-day temporal

301   resolution (Table1). The observed white-sky albedo was used as the daytime albedo (Peng et

302   al., 2014). For evapotranspiration (ET), we used the ET band in MOD16A2, which includes

303   water fluxes from soil evaporation, wet canopy evaporation and plant transpiration. To calculate

304   the mean annual albedo and evapotranspiration for 2002–2004 (t_1) and 2010–2014 (t_2) we used

305   the same approach as used for LST.

306

307   2.2.3 Land-Cover Datasets and Processing

308

309   Two land-cover datasets were used in this study: the 'actual effect' approach was based on the

310   Global Forest Change (GFC) dataset, while the 'mixed potential effect' and 'full potential effect'

311   used the GlobeLand30 land-cover data (Table 1).

312

313   The SVD technique, used in the 'full potential effect' approach, requires a land-cover map with

314   a higher spatial resolution than the 1km spatial resolution of the LST data. The GlobeLand30

315   product, which is based on Landsat images, provides land-cover information for China at a 30m

316   resolution for the years 2000 and 2010 (Chen et al., 2015). Cultivated land and grassland in

317   GlobeLand30 were classified as openland. Discrete land-cover type information at 30m

318   resolution in 2010 was aggregated to obtain the area fractions of the different land-cover types

319   at 1km resolution, which were then used to construct matrix X in Eq. (5) (Fig. 2). Furthermore,

320   land-cover type information at the 1km scale was extracted, based on the vegetation type with

321   area fraction >50% for every 1km×1km window. This data was then applied in the 'space-for-

322   time' method to identify forest and openland (Fig. 2).

323

324   GlobeLand30 data is not suitable for detecting forest change (Zeng et al., 2021). The Global

325   Forest Change (GFC) data, however, provides forest gain and forest loss at a spatial resolution

326   of 30m between 2000 and 2012 and has been used for mapping global forest change (Hansen

327   et al., 2013). This product shows an overall accuracy of greater than 99% for areas of forest

328   gain at the global scale when compared with statistical data reported in Forest Resource

329   Assessment (FRA), LiDAR detection (Geoscience Laser Altimetry System), and MODIS

330   NDVI time series (Hansen et al., 2013), and thus has been recommended for use in forest and

331   forest-change estimates (Chen et al., 2020; Zeng et al., 2021). Using this dataset, forest loss

332   events were identified for each year between 2000 and 2012, but forest gain was only identified

333   for the whole period, simply because forest loss is an abrupt change which can be effectively

334   identified over short time periods, whereas forest gain is a gradual change which can only be

335   confidently identified over longer time spans. Here, forest losses and gains from GFC were

336   aggregated at a 1km resolution to obtain net forest change (defined as forest gain minus forest

337   loss) during this period (Fig. 2). A positive net change indicates afforestation and the area

338   percentage of afforestation for the 1km pixel area was defined as F_{aff}. The land-cover type of

339   pixels with $F_{aff} = 0\%$ was considered to be stable. This net forest-change information was then

340   used in the calculation of the actual afforestation-induced temperature effect (ΔT_a)(Fig. 2).

341

342   2.3 Decomposition of Changes in Surface Temperature

343

344   Changes in surface temperature following forest-cover change are the net result of changes in

345   underlying fluxes that collectively determine the land surface energy balance:

346   $$\Delta SW_{in} - \Delta SW_{out} + \Delta LW_{in} - \Delta LW_{out} = \Delta H + \Delta LE + \Delta G \tag{11}$$

347   where ΔSW_{in}, ΔSW_{out}, ΔLW_{in}, ΔLW_{out} are the changes in incoming and outgoing shortwave

348   and longwave radiation, respectively, and ΔH, ΔLE, and ΔG are changes in sensible heat flux,

latent heat flux and ground heat flux, respectively. All the terms of Eq. (11) are expressed in Wm^{-2}.

Firstly, it can be reasonably assumed that $\Delta SW_{in} \approx 0$ and $\Delta LW_{in} \approx 0$, given that all three approaches consider only local effects on surface temperature by following a comparison of target pixels with surrounding control pixels, thus excluding feedbacks from, e.g., cloud formation (Duveiller et al., 2018). Changes in reflected shortwave radiation can be derived as:

$$\Delta SW_{out} = SW_{in} \times \Delta \alpha \tag{12}$$

where SW_{in} is available from the CERES EBAF-Surface Product Ed 4.1 (Kato et al., 2018; Liu et al., 2018) (Table 1), and $\Delta \alpha$ is the surface albedo change. To approximate ΔLW_{out}, we used its first order differential equation:

$$\Delta LW_{out} = \sigma(4\varepsilon_B T^3 \Delta T + \Delta \varepsilon_B T^4) \tag{13}$$

where σ is Stefan-Boltzmann's constant (5.67×10^{-8} W m^{-2} K^{-4}), T is daytime surface temperature and ΔT is the afforestation impact on surface temperature. Surface broadband emissivity, ε_B, is usually obtained from an empirical relationship (Zhang et al., 2019):

$$\varepsilon_B = 0.2122\varepsilon_{29} + 0.3859\varepsilon_{31} + 0.4029\varepsilon_{32} \tag{14}$$

where ε_{29}, ε_{31} and ε_{32} are obtained from the estimated emissivity for bands 29 (8,400–8,700 nm), 31 (10,780–11,280 nm) and 32 (11,770–12,270 nm) in the MOD11C3 data (Duveiller et al., 2018).

Latent heat flux change (ΔLE) refers to changes in the energy used for evapotranspiration (ET, unit: mm d^{-1}), which can be obtained from the change in evapotranspiration (ΔET):

$$\Delta LE = \Delta ET \times 28.94 \text{ W m}^{-2}/(\text{mm d}^{-1}) \tag{15}$$

Therefore, the sum of sensible heat change and ground heat change ($\Delta H + \Delta G$) can be calculated as the difference between net radiation change and latent heat flux change (ΔLE) based on Eq.

374   (11). The afforestation effects on albedo ($\Delta\alpha$), ε_B ($\Delta\varepsilon_B$) and ET (ΔET) needed in the above

375   equations were calculated in a similar way to ΔT for each of the three different approaches as

376   described in Section 2.1.

377

378   2.4 Statistical Analysis

379   The spatial distributions of original samples for the three methods are different because of the

380   different land-cover maps used (Fig. 2 and Figure A1) and, therefore, the statistical analysis

381   was limited to those pixels shared by all three approaches: 96,058 sample pixels at 1km

382   resolution. The distribution of these shared sample pixels retained the characteristics of the

383   spatial distribution of the original samples (Figure A2).

384

385   Differences in the afforestation effects on LST of the three approaches were tested by

386   performing paired-samples *t*-tests between pairs of approaches. The paired-samples *t*-test was

387   used, rather than a normal *t*-test, to avoid the bias due to strong spatial heterogeneity in the LST

388   effects of afforestation that could occur if the values of all pixels had been pooled together for

389   a normal *t*-test. The test was made using the 'ttest_rel' method from the 'scipy.stats' package

390   in Python. The Bonferroni correction was applied to adjust the significance level (p-value) to

391   mitigate the increasing Type I error when making multiple paired-samples *t*-test, which in our

392   case involves three pairs (Lee and Lee, 2018; UC Berkely, 2008). The Bonferroni correction

393   sets the significance cut-off at α/k (with α as the p-value before correction and k as number of

394   pairs). In this study, with 3 hypotheses tests (i.e., 3 pairs) and an original significance level $\alpha =$

395   0.05, the adjusted p-value is 0.0167. In order to investigate ΔT_a in relation to the afforestation

396   intensity, a linear regression was performed between ΔT_a and F_{aff} using the ordinary least

397   squares method.

398

399 Table 1 Summary of the datasets and their main characteristics

Type	Dataset	Selected band	Resolution	Projection	Timespan
Forest change	Global Forest Change	Forest gain; Loss year	30m, annual	WGS84	2000–2012
Land-cover type	GlobeLand 30	Land-cover type	30m, —	UTM	2000; 2010
Land surface Temperature	MOD11A2	Daytime temperature	1km, 8days	sinusoidal	2002–2004; 2010–2014
Albedo	MCD43B3	Albedo WSA shortwave	1km, 16days	sinusoidal	2002–2004; 2010–2014
Incoming shortwave radiation	CERES	sfc_sw_down _all_mon	1°, monthly	WGS84	2002–2004; 2010–2014
Surface broadband emissivity	MOD11C3	Emis_29; Emis_31; Emis_32	0.05°, monthly	sinusoidal	2002–2004; 2010–2014
Evapotranspiration	MOD16A2	ET_500m	500m, 8days	sinusoidal	2002–2004; 2010–2014
Elevation	SRTM30	Be75	30m, —	WGS84	—

400

3 Results

3.1 Spatial Distribution of Afforestation and its Effect on Land Surface Temperature

In China, afforestation areas are mainly located in the northeast, southwest and south, where sufficient precipitation is available (Fig. 3a) and largely driven by afforestation of former cropland or abandoned cropland, with a relatively small contribution from forest regeneration or replanting following natural disturbance or timber harvest. One prominent feature of afforestation in China is its small afforestation patch, with most afforested pixels ($1km^2$) having an afforestation fraction of less than 30% (Fig. 3b). Pixels with an afforestation intensity below 10% account for 93% of the total number of pixels (Fig. 3b), representing 0.14 Mha, more than half (55.6%) of the total afforestation area (Fig. 3b).
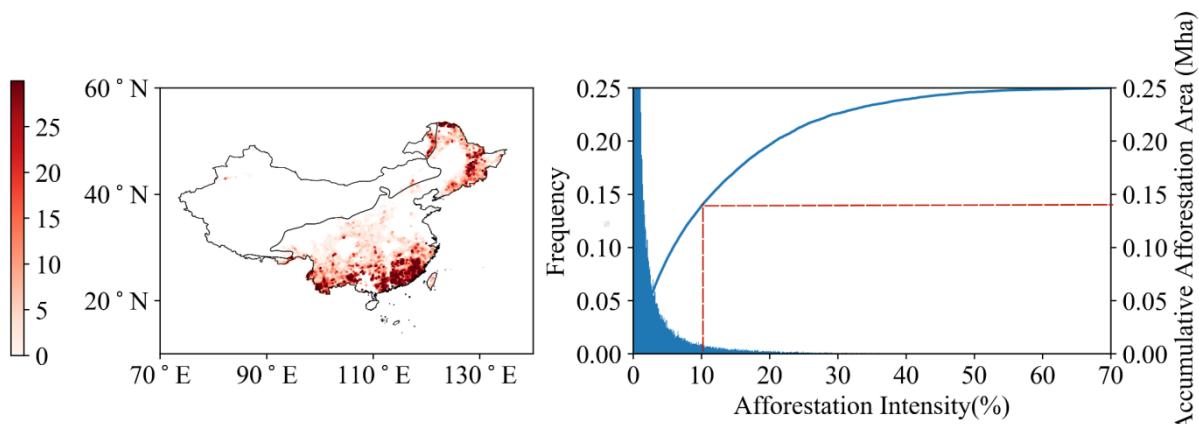
Figure 3. (a) Spatial distribution of afforestation intensity (F_{aff}) in China during 2000–2012. The solid black line crossing China is the 400mm annual precipitation isoline. (b) Frequency distribution of F_{aff} and cumulative afforestation area with the increase in F_{aff}. The red dashed line represents the cumulative afforestation area corresponding to $F_{aff} = 10\%$.

419   Although all three approaches result in similar spatial and latitudinal patterns regarding

420   afforestation effects on LST (Fig. 4), their magnitudes differ substantially. The actual effect has

421   the lowest temperature change, followed by the mixed potential effect, with the full potential

422   effect showing the greatest temperature change (Fig. 4a–c). For the latitude range of 20–36° N

423   where afforestation effects show a dominant cooling effect, the full potential effect (ΔT_{p2})

424   reaches -1.75±0.01K, while the mixed potential effect (ΔT_{p1}) was smaller at -0.96±0.00K, but

425   both of them were much larger than the actual effect (ΔT_a) of -0.09±0.00K. Similarly, the full

426   potential effect (ΔT_{p2}) showed the strongest warming effect (0.35±0.01K) in the area north of

427   48° N, stronger than the mixed potential effect (0.22±0.01K), and again the actual effect is the

428   smallest (0.07±0.01K). However, regarding the latitude where the effects change from a

429   warming to cooling effect, the three approaches largely converge (Fig. 4d). Between 40° N and

430   48° N, the afforestation effects are largely neutral, with the mean temperature change for the

431   three approaches being 0.07±0.01K (ΔT_a=-0.01±0.01K; ΔT_{p1}=0.11±0.01K; ΔT_{p2}=0.12±0.01K).
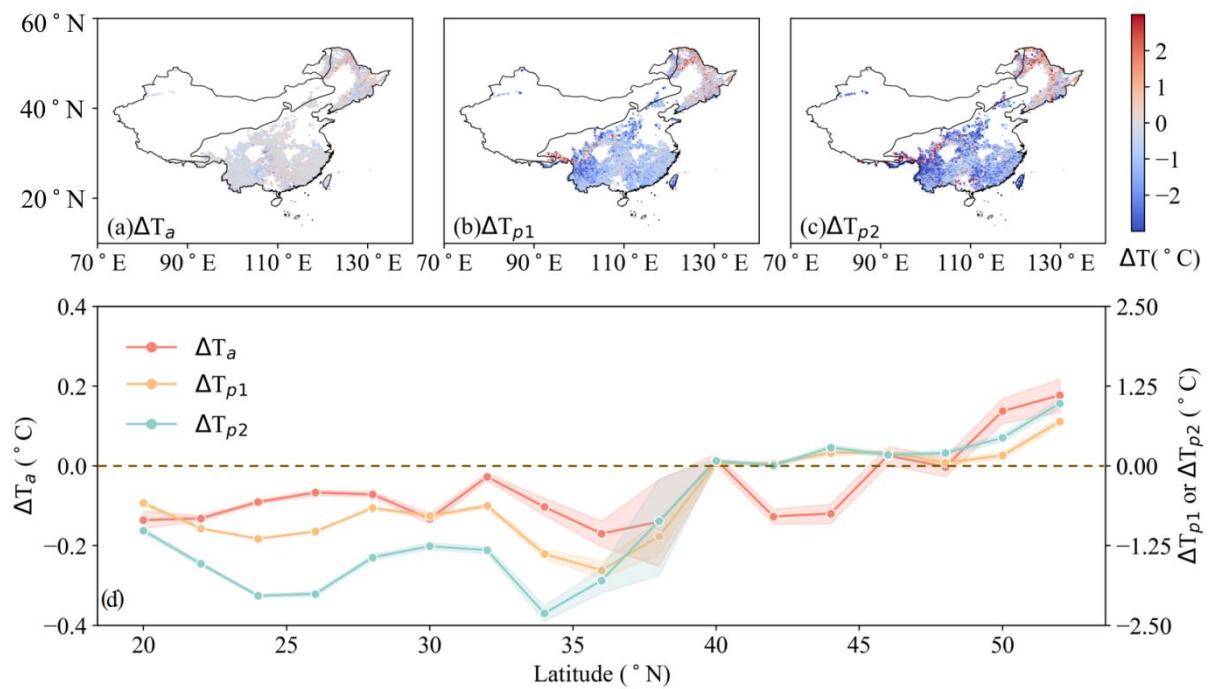
432

433   **Figure 4.** Afforestation effects on LST quantified by three approaches: (a) actual effect based

434   on a 'space-and-time' approach (ΔT_a), (b) mixed potential effect based on a 'space-for-time'

approach (ΔT_{p1}) and (c) full potential effect assuming a transition from 100% openland coverage to 100% forest coverage using the SVD method (ΔT_{p2}). The solid black line crossing China is the 400mm precipitation isoline. (d) Zonal averages of the annual mean daytime LST change within 2° latitudinal bins, with shaded areas representing the standard errors (SE). Note that in panel (d), ΔT_a corresponds to the vertical axis on the left; ΔT_{p1} and ΔT_{p2} correspond to the vertical axis on the right.

3.2 Reconciling Temperature Effects of Afforestation

Even though the observed land surface temperature is assumed to be uniform for the 1km afforested satellite pixel, the underlying afforestation intensity varies substantially (Fig. 3a). This leads to our first hypothesis that for a 1km pixel, ΔT_a should be influenced by the area fraction that has been afforested within the pixel (i.e., afforestation intensity or F_{aff}). Indeed, the actual daytime surface cooling increases significantly with afforestation intensity (Fig. 5), with a 0.079±0.017K (mean ± std) increase for each ten percent increase in F_{aff}.
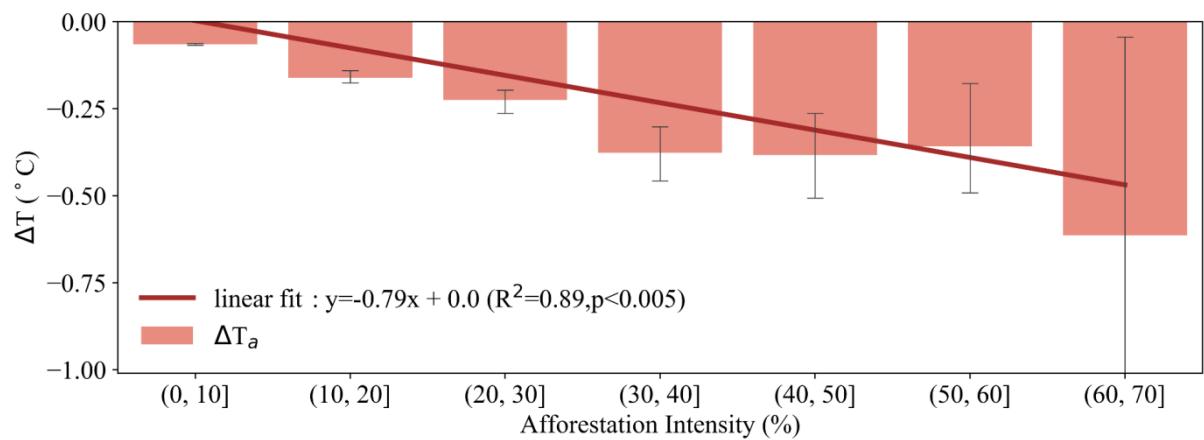
Figure 5. Changes in ΔT_a as a function of afforestation intensity (F_{aff}), defined as the fraction of afforested area to the total pixel area at a 1-km resolution. Error bars indicate the standard error of ΔT_a within each ten percent bin of F_{aff}. The red line represents the fitted linear regression line between ΔT_a and F_{aff}.

455

456 The afforestation effects obtained from the three approaches were compared for each F_{aff}

457 interval (Fig. 6). When afforestation intensity is less than 60%, significant differences exist in

458 the temperature change obtained by the three approaches, with $\Delta T_a < \Delta T_{p1} < \Delta T_{p2}$. This result

459 confirms our second hypothesis that the actual effect is expected to be smaller than potential

460 effects. However, for pixels with relatively low F_{aff}, the mixed potential effect is found to be

461 smaller than the full potential effect, which is reasonable, but to our knowledge, has not been

462 reported before. When the afforestation intensity is greater than 60%, the significant difference

463 in cooling effect between the different approaches disappears, likely because afforestation

464 intensity, and the associated forest coverage at 1km resolution, reach values high enough to

465 allow the 'potential' effects to be realized.
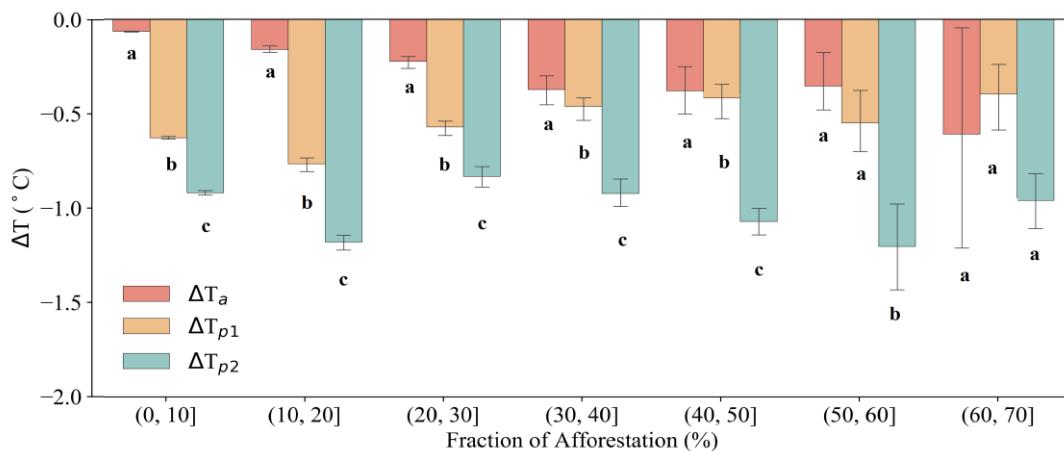
466 **Figure 6.** Comparison of ΔT for the three approaches for bins of afforestation intensity. Error

467 bars are given as the standard error and different letters indicate that ΔT calculated by the two

468 approaches concerned are significantly different using the adjusted p-value after applying the

469 Bonferroni correction for multiple paired-samples *t*-tests.

470

471 When considering the overall differences in ΔT for the three approaches, irrespective of the

472 afforestation intensity, ΔT_a (-0.07±0.00K) over China was significantly lower than ΔT_{p1} (-

473 0.63±0.00K), which is further significantly lower than ΔT_{p2} (-1.16±0.01K) (p < 0.05, paired-

474   samples t-test, n= 96,058), once again confirming our second hypothesis (Fig. 7). Moreover,

475   extrapolation of the relationship shown in Fig. 5 suggests that ΔT_a would reach -0.79±0.17K

476   (mean ± std) if a 1km pixel was 100% afforested, which is conceptually comparable to the

477   potential effects. ΔT_a was indeed found to be higher than ΔT_{p1} but lower than ΔT_{p2}. This result

478   confirms our third hypothesis and demonstrates that the potential cooling effect could indeed

479   be reached when a pixel is fully afforested.

480
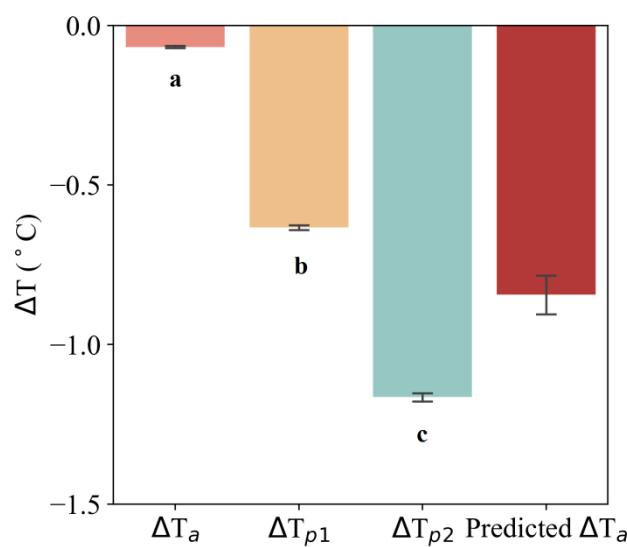
481   **Figure 7**. Comparison of ΔT for the three approaches, irrespective of the afforestation intensity.

482   Error bars are given as the standard error and different letters indicate ΔT being significantly

483   different (p = 0.0167, paired-samples t-test, n = 96,058). For comparison, the predicted ΔT_a

484   with F_{aff} reaching 100%, which is conceptually comparable with ΔT_{p1} and ΔT_{p2}, is also shown.

485

486   3.3 Reconciling Changes in Surface Energy Fluxes by Afforestation

487

488   In order to investigate whether the underlying surface energy fluxes could be reconciled

489   following the reconciliation of the LST changes, changes in surface energy fluxes due to

490   afforestation were quantified using each of the three approaches, under the same boundary

491 conditions as for full afforestation (i.e., changes following the 'actual effect' approach were

492 extended for $F_{aff} = 100\%$). As illustrated in Fig. 8, changes in all the relevant surface energy

493 fluxes under the three different approaches have the same direction, with similar magnitudes,

494 confirming the reconciliation of the different approaches in terms of surface energy fluxes.

495 More specifically, the three approaches converge on a reduction in reflected shortwave

496 radiation (ΔSW_{out}) of 0.56~1.23 W m^{-2} due to the lower albedo of forest compared to openland

497 (Figure A3). Emitted longwave radiation (ΔLW_{out}) was reduced by 1.03~3.10 W m^{-2} and

498 sensible and ground heat fluxes ($\Delta H+\Delta G$) reduced by 4.84~6.14 W m^{-2}. All these reduced

499 fluxes were offset by an increased latent heat flux of 7.99~8.41 W m^{-2} (ΔLE), the single energy

500 flux leading to surface cooling.
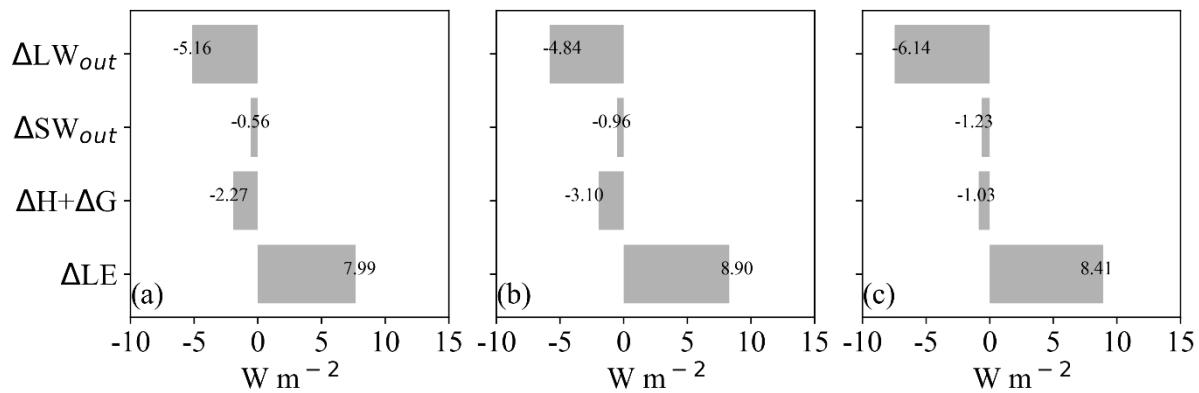
501

502 **Figure 8.** Afforestation-induced changes in surface energy fluxes (Wm^{-2}) following the three

503 approaches: (a) actual effect based on a 'space-and-time' approach, (b) mixed potential effect

504 using medium-resolution land cover maps based on a 'space-for-time' approach and (c) full

505 potential effect assuming a transition from 100% openland coverage to 100% forest coverage

506 using the SVD method. For each approach, changes were calculated for the reflected shortwave

507 radiation (SW_{out}), outgoing longwave radiation (LW_{out}), latent heat flux (LE) and the

508 combination of sensible and ground heat fluxes (H+G). No changes were assumed for incoming

509 shortwave and longwave radiation. Changes in energy fluxes for the 'actual effect' approach

510 have been adjusted to the condition of full afforestation (i.e., $F_{aff} = 100\%$) in a similar way as

511   for the 'predicted ΔT_a' in Fig. 7, by fitting linear regressions between energy flux variables and

512   F_{aff} (Figure A4).

513

514   ## 4 Discussion

515

516   The three approaches (Li et al., 2015; Alkama and Cescatti, 2016; Duveiller et al., 2018) used

517   to quantify local surface temperature change following forest-cover change and presented with

518   details in this study, have been cited over 919 times in research papers (Web of Science,

519   December 2021) and in high-level climate science synthesis reports. Despite the apparently

520   large differences in temperature effect among them, to our knowledge, no studies have

521   examined whether these differences can be reconciled. This study fills that gap by comparing

522   the three approaches for a single study case, i.e., large-scale afforestation in China. China is

523   highly suitable for the purpose of this study as the size of an afforestation patch is, in general,

524   smaller than the spatial resolution (1km) at which the temperature effects of afforestation were

525   conducted in the previous studies describing the three approaches (Li et al., 2015; Alkama and

526   Cescatti, 2016; Duveiller et al., 2018). Hence, the difference between the actual and potential

527   temperature effects is expected to be large.

528

529   Indeed, we found surface cooling following afforestation was much less when estimated as the

530   actual effect (ΔT_a) compared to the potential effects (ΔT_{p1} and ΔT_{p2}). This lower ΔT_a has been

531   attributed to incomplete afforestation at a 1km resolution, at which potential effects are

532   quantified by assuming complete afforestation (i.e., a complete shift from openland to forest).

533   Consistent with our first hypothesis, the afforestation fraction at a 1km resolution explained 89%

534   of the variation in ΔT_a, making it a key determinant of the surface cooling following

535   afforestation (Fig. 5). This result is consistent with the fact that the observed temperature for a

536   mixed surface is determined by the area fractions of its respective components, with each

537   component having a unique temperature. This fact also forms the theoretical foundation for the

538   SVD technique used to derive the full potential effect (Duveiller et al., 2018).

539

540   Modelling (Li et al., 2016b) and satellite-based (Alkama and Cescatti, 2016) studies have found

541   that temperature change after afforestation (or deforestation) is highly sensitive to the fraction

542   of the model grid cell or satellite pixel that is subjected to afforestation (or deforestation),

543   echoing our finding that ΔT_a significantly changes with F_{aff}. In addition, we provide strong

544   evidence in support of our third hypothesis that when F_{aff} reaches 100%, the expected actual

545   effect is comparable to the potential effects (Fig. 7). This finding shows that the three

546   approaches compared here are consistent when the same boundary condition, i.e., full

547   afforestation, is applied, and demonstrates that all three methods are mutually compatible. It is,

548   therefore, the basis of the reconciliation of the three approaches. It also highlights the fact that

549   the actual afforestation area must be considered when evaluating the climate mitigation effects

550   of afforestation.

551

552   Our results also show that the mixed potential effect (ΔT_{p1}) is smaller than the full potential

553   effect (ΔT_{p2}) (Fig. 6, Fig. 7). We suspect that this phenomenon likely also relates to the

554   incomplete forest coverage for the identified forest pixels at the 1km scale used in the 'space-

555   for-time' analysis, because a threshold value of 50% forest cover was used when upscaling the

556   30m land-cover map to 1km resolution. This threshold, however, is consistent with the

557   commonly applied value in land-cover classification based on medium resolution satellite

558   images, such as MCD12Q1, which uses a tree coverage value of 60% to identify forest pixels

559   (Sulla-Menashe and Friedl, 2018). For the purpose of comparison, we also calculated the mixed

560   potential effect based on the MCD12Q1 land-cover map but using the same LST data. The

561   result shows that potential effects derived using MCD12Q1 data versus those derived using

562   spatially upscaled GlobeLand30 data are almost identical (Figure A5), lending credibility to our

563   estimated ΔT_{p1} in comparison to previous studies using MODIS land-cover data (Li et al., 2015).

564   Progressively increasing the forest-cover threshold from 50% to 90% steadily increases ΔT_{p1}

565   from -0.62±0.02K to -0.75±0.02K (Figure A6). Further increasing the thresholds used to

566   identify 1km-resolution openland pixels from 50% to 90% increases ΔT_{p1} from -0.63±0.00K to

567   -1.10±0.02K (Figure A7), bringing ΔT_{p1} even closer to ΔT_{p2} (-1.16±0.01K). This is consistent

568   with the finding of a previous study on the dependence of the temperature effect on the forest

569   cover change thresholds that were used to define afforestation: the higher the threshold, the

570   stronger the impact on temperature (Li et al., 2016). Our results add further support to the

571   compatibility of the three approaches given the same boundary condition, i.e., the complete

572   transformation from full openland to full forest coverage.

573

574   Several factors may contribute to the remaining differences in the temperature effects produced

575   by different methods even after reconciliation. As described in the Method section, there are

576   discrepancies in the assumptions of the three approaches, which lead to differences in the

577   control pixels (i.e., adjacent comparison pixels). For instance, for the 'pure potential effect' it

578   is assumed that the LSTs for pixels with the same land cover type are uniform and forest pixels

579   are compared with openland pixels, whereas the in the 'mixed potential impact' approach the

580   central target forest pixel is compared with the mean value of non-forest pixels within the

581   searching window. Moreover, space-for-time is an assumption that cannot be verified (Chen et

582   al., 2016), and which will inevitably result in differences in the estimated actual and potential

583   effects, although the consistency between 'potential' and 'actual' effects after reconciliation in

584   our study does illustrate the broad validity of this assumption.

585

586 Differences between the actual and potential temperature effects can also arise from influences

587 of both the timing of the afforestation and the time period elapsed following afforestation.

588 However, such influences are expected to be small in our study. We argue that such influences

589 should be more pronounced in the case of deforestation than afforestation. The temperature

590 effect caused by deforestation is considered to be instant (Liu et al., 2018). As a result, if

591 deforestation occurred in one specific year of our starting time window (i.e., 2002–2004), using

592 the time-averaging LST over the whole time window to represent the LST before deforestation

593 will greatly bias the quantified ΔT. In contrast, afforestation-driven surface temperature change

594 can only gradually increase with forest development. The LST effect depends on different

595 stages of forest development and is expected to saturate only when the forest canopy stabilizes

596 (Zhang et al., 2021; Windisch et al., 2021). Observation studies show that closed dense-canopy

597 old forests can exert greater cooling effect than the open-canopy young forests (Zhang et al.,

598 2021; Windisch et al., 2021). Hence, given the gradual nature of the afforestation effect on LST,

599 when we quantify the afforestation effect by comparing the time-averaging LST before and

600 after afforestation, the influence of the specific 'timing of afforestation' is expected to be small.

601 Furthermore, the GFC dataset used in this analysis defined forest gain using the condition of

602 successful detection of a stable closed forest canopy that is clearly different from a non-forest

603 state (Hansen et al., 2013), which enhances the chance of temperature change saturation

604 following afforestation. But, given a maximum stand age of 12 years inferred from the GFC

605 dataset, differences in surface temperatures may still exist between newly established forests

606 and the mature existing forests that were used in the 'potential effect' approaches. Thus, we

607 cannot exclude the possible contribution of time period elapsed following afforestation to the

608 difference between the actual and potential effects, which failed to be reconciled.

609

610   Previous analyses have documented latitudinal patterns of surface temperature change induced

611   by afforestation (Alkama and Cescatti, 2016; Li et al., 2015, 2016a; Peng et al., 2014). When

612   comparing the three approaches for a single case study, consistent latitudinal patterns of local

613   surface temperature effects following afforestation are observed (Fig. 4). Notably, all three

614   approaches show a warming effect in the northern high latitudes and an opposite cooling effect

615   in the southern low latitudes, with a largely neutral effect in the 40–48° N latitude band,

616   providing further evidence that the three approaches are compatible. In particular, although the

617   three approaches used different land-cover maps, they derived consistent LST impacts

618   following afforestation, which highlights that fact that the reconciliation provided in this study

619   is rather robust and unlikely to be dependent on the land cover datasets used.

620

621   In addition to the reconciliation of the land surface temperature change, we checked and

622   confirmed that the changes in surface energy fluxes that underlie and drive the changes in

623   surface temperature are compatible under the boundary condition of full afforestation. This

624   finding confirms the inherent consistency in the three approaches and clarifies the reasons

625   behind the apparent discrepancies in existing studies as discussed in the introduction.

626   Nonetheless, when it comes to the biophysical impacts of afforestation in the real world, our

627   findings have far-reaching implications. Full afforestation is often possible at small spatial

628   scales but becomes challenging at large scale. Therefore, the realization of the full potential

629   effect by afforestation is scale-dependent. For example, a complete afforestation of the semi-

630   arid Loess Plateau in the northwest of China is predicted to generate a surface cooling effect of

631   2.40 ± 0.07K, but substantial afforestation efforts over the past 4 decades in that region have only

632   realized a cooling of 0.11 ± 0.01K as measured by the 'actual effect'. Because of greater water

633   consumption by forest compared to openland and the need to maintain land area for food

634   production, achieving the full cooling potential may not be feasible (Huang et al., 2018; Liu

635   and She, 2012; Liang et al., 2019).

636

637   Potential cooling effects have a value in that they can serve to establish the envelope of effects

638   and measure possible outcomes given the condition of full afforestation. However, given the

639   challenge of full afforestation at large spatial scales, potential effects should be converted into

640   a more realistic estimate (i.e., actual effects), by taking into account the intensity of afforestation,

641   to better represent policy ambitions. The analog could also be made for the effects of the surface

642   energy impacts of afforestation. Taking 10% as the afforestation intensity threshold to compare

643   the cumulative surface energy effect between the actual and potential approaches, actual

644   cumulative biophysical changes (5.06 EJ) for 2000–2012 are much smaller than mixed potential

645   changes (20.13 EJ) and full potential change (19.02 EJ) (methods in Text A1; Figure A8). Again,

646   this shows that simply using the potential effects for policy making or evaluation risks greatly

647   overestimating the biophysical effects of afforestation.

648

649   5 Conclusions

650   In this study we provided a synthesis of the three influential methods used to quantify

651   afforestation impact on surface temperature change and provided evidence that these different

652   methods could in fact be reconciled. The actual effect of surface temperature change following

653   afforestation was highly dependent on the intensity of afforestation (F_{aff}), which explained 89%

654   of the variation in ΔT_a. With the common boundary condition of full afforestation being applied,

655   differences in afforestation impacts on LST reported by the three methods in previous studies

656   greatly reduced, showing that simply treating these differences as uncertainty is incorrect and

657   could greatly overestimate the uncertainty. In other words, when full afforestation is assumed,

658   the actual effect approaches the potential effect, demonstrating the effectiveness of the 'space-

659   for-time' approach and that the potential cooling effect of afforestation could indeed be realized.

660   Potential cooling effects have a value in academic studies where they can be used to establish

661   an envelope of effects, but their realization at large scales is challenging given the scale

662   dependency. The reconciliation of the different approaches demonstrated here stresses that the

663   afforestation fraction should be accounted for in order to bridge different estimates of surface

664   cooling effects in policy evaluation.

665

666   **Appendix A**
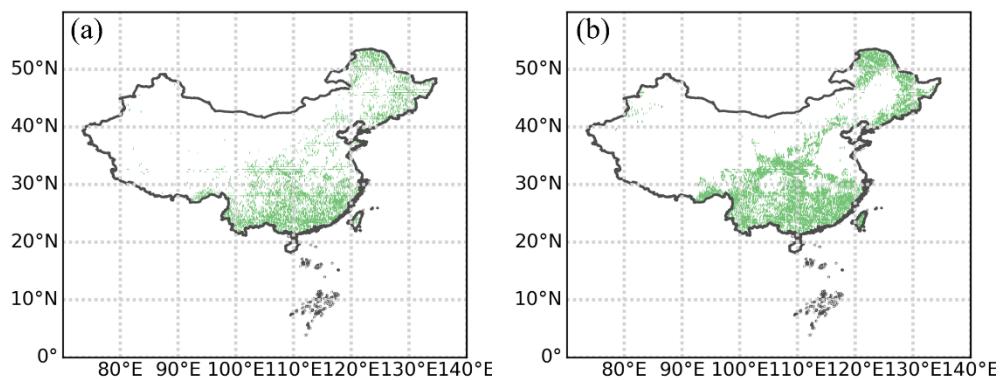
667   **Figure A1.** The distributions of the original sample pixels (at a 1km resolution) for (a) the

668   actual effect and (b) the two potential effects.
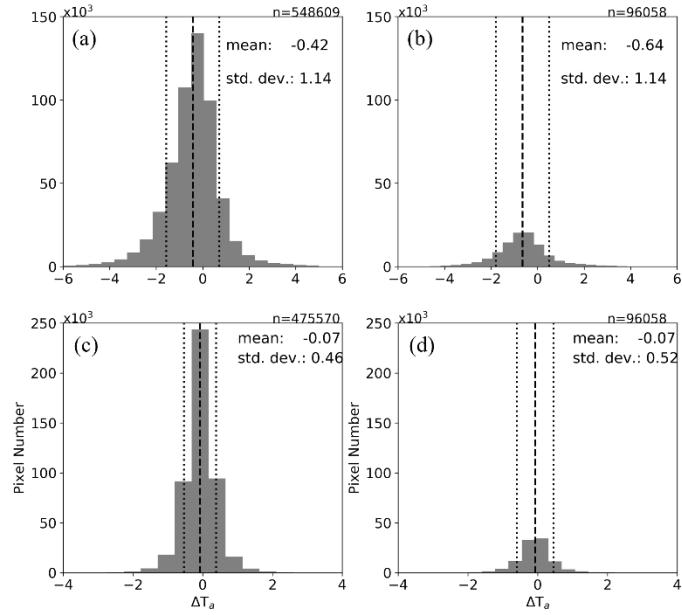
Figure A2. (a) Histogram of ΔT_a of all pixels based on the GFC dataset (b) Histogram of ΔT_a for samples used for the statistical test. (c) Histogram of ΔT_{p1} of all pixels based on GFC dataset (d) Histogram of ΔT_{p2} for samples used for the statistical test.
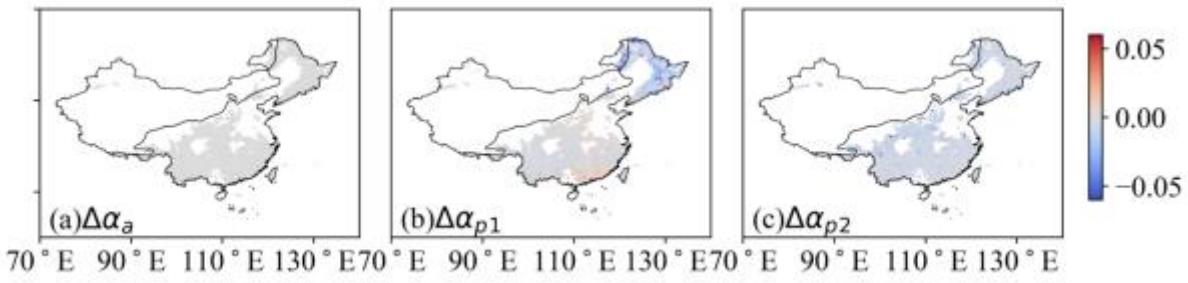
Figure A3. Spatial distribution of afforestation-induced changes in albedo (α) over China from three approaches: (a) Actual albedo change following afforestation based on 'space-and-time' method ($\Delta\alpha_a$), (b) mixed potential albedo change using medium-resolution land-cover maps based on 'space-for-time' approach ($\Delta\alpha_{p1}$) and (c) full potential effect ($\Delta\alpha_{p2}$) based on SVD approach.
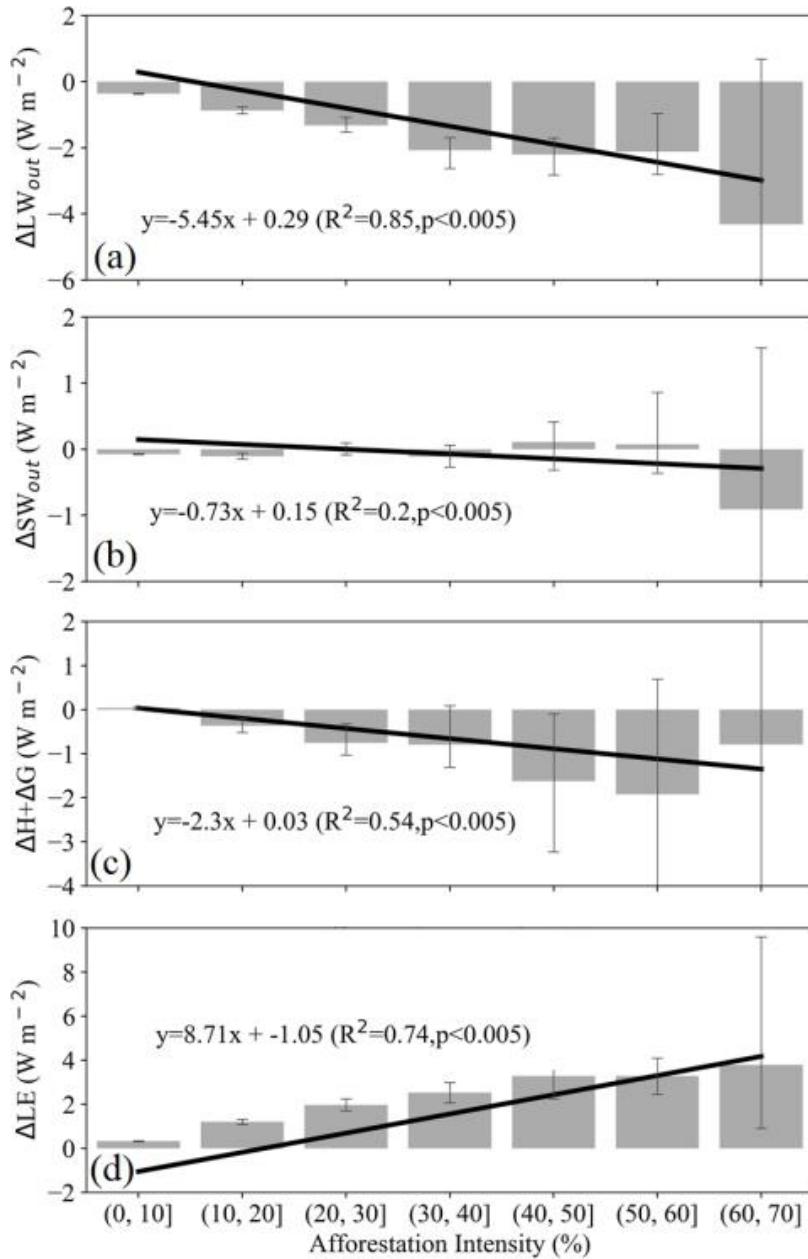
Figure A4. Changes of actual effect in (a) ΔLW, (b) ΔSW, (c) $\Delta H+\Delta G$ and (d) ΔLE (W m^{-2}) as a function of afforestation intensity (F_{aff}) following the 'actual effect' approach. Error bars indicate the standard error within each ten percent bin of F_{aff}. The solid black lines represent the fitted linear regression line between each energy flux variable and F_{aff}.
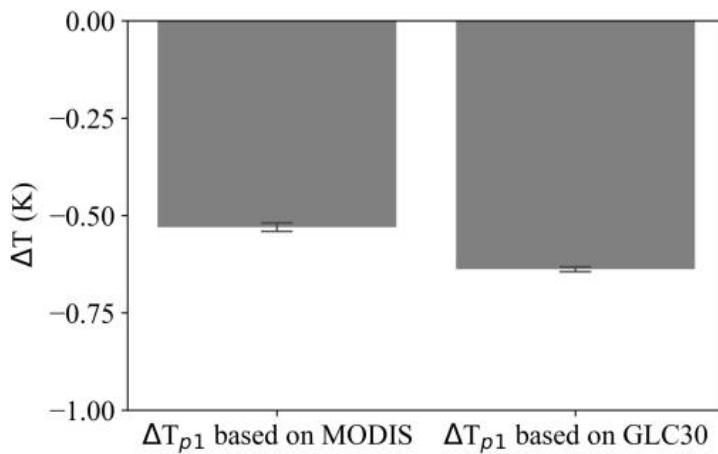
689   **Figure A5.** The mixed potential effects (ΔT_{p1}) obtained based on MODIS land-cover data

690   (MCD12Q1) and the land-cover distribution map defined at the threshold of 50% GlobeLand30

691   at 1 km resolution.

692
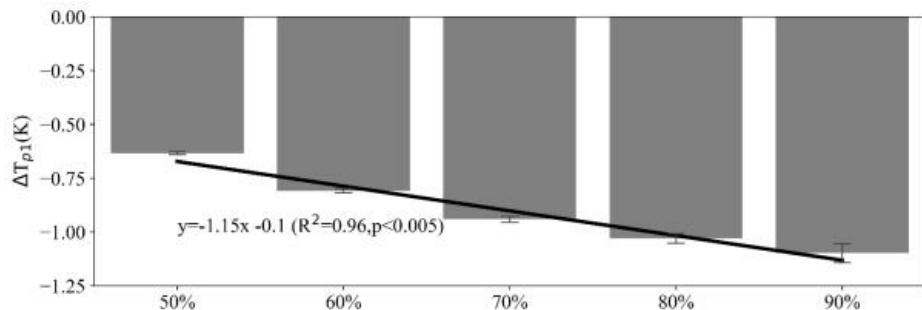
693   **Figure A6.** The influence of the forest-cover threshold applied to the land-cover map

694   underlying the estimation of the mixed potential effect (ΔT_{p1}).

695
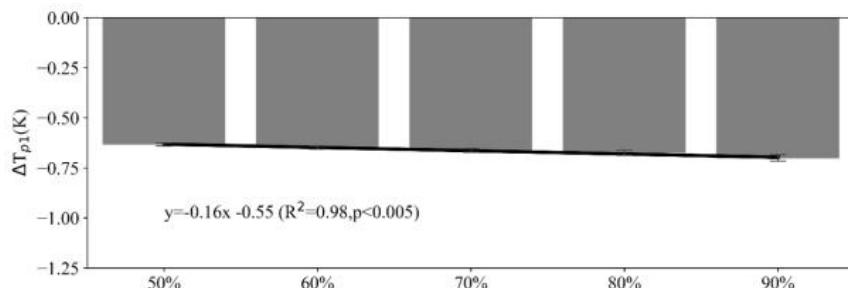
696   **Figure A7.** The influence of the openland-cover threshold used to identify a 1km pixel as

697   openland in the estimation of the mixed potential effect (ΔT_{p1}).

698
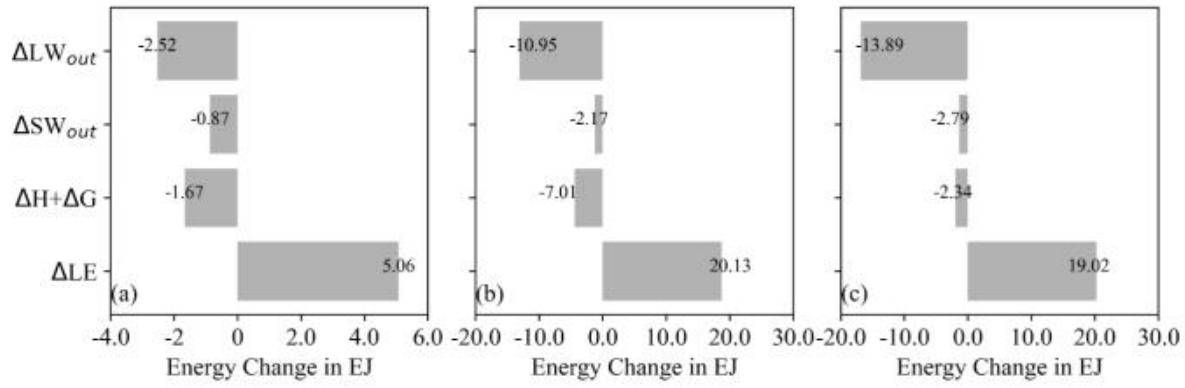
Figure A8. Afforestation-induced cumulative changes in surface energy fluxes (exaJoules) in

China for the period 2000–2012 following the approaches of (a) actual effect, (b) mixed

potential effect and (c) full potential effect (methods in Appendix Text A1).

702

Text A1

The cumulative surface energy effect (f_{cum}) in Figure A8 refers to the sum of the flux change (J)

from all the samples, while at the same time accounting for the forest change area (m^2). More

specifically, the cumulative surface energy change (f_{cum}) can be calculated from equation A1:

$$f_{cum} = \sum_{i=1}^{i=n}(area_i \times F_i)$$
(A1)

where F_i is the flux change per unit area (W m^{-2}) for pixel i, n is the total number of samples,

and $area_i$ is the forest change area in pixel i.

710

Data availability

All datasets used in this study are summarized in Table 1 and are openly available. Albedo,

transpiration and surface temperature data can be accessed at

(https://modis.gsfc.nasa.gov/data/). The Global Forest Change data is available from

https://earthenginepartners.appspot.com/science-2013-global-forest/. The land-cover type

dataset (GlobeLand30) can be downloaded from http://www.globallandcover.com/. Incoming

shortwave radiation data can be accessed at https://ceres.larc.nasa.gov/data/. The elevation data is available from NASA's Shuttle Radar Topography Mission (SRTM) data (https://lpdaac.usgs.gov/products/srtmgl1v003/). Intermediate data and scripts used to generate the results in this study are available from the corresponding author upon reasonable request.

Author contributions

Chao Yue and Sebastiaan Luyssaert designed the study. Huanhuan Wang conducted the analysis. All three authors contributed to writing and revision of the text.

Competing interests

The authors have the following competing interests: At least one of the (co-)authors is a member of the editorial board of Biogeosciences.

Acknowledgments

This study was supported by the Strategic Priority Research Program of the Chinese Academy of Sciences (grant no. XDB40020000) and by the National Natural Science Foundation of China (grant no. 41971132).

References

Alkama, R. and Cescatti, A.: Biophysical climate impacts of recent changes in global forest cover, Science, 351, 600–604, https://doi.org/10.1126/science.aac8083, 2016.

Bonan, G. B.: Forests and climate change: forcings, feedbacks, and the climate benefits of forests, Science, 320, 1444–1449, https://doi.org/10.1126/science.1155121, 2008.

Bryan, B. A., Gao, L., Ye, Y., Sun, X., Connor, J. D., Crossman, N. D., Stafford-Smith, M., Wu, J., He, C., Yu, D., Liu, Z., Li, A., Huang, Q., Ren, H., Deng, X., Zheng, H., Niu, J.,

Han, G., and Hou, X.: China's response to a national land-system sustainability emergency, Nature, 559, 193–204, https://doi.org/10.1038/s41586-018-0280-2, 2018.

Chen, C., Park, T., Wang, X., Piao, S., Xu, B., Chaturvedi, R. K., Fuchs, R., Brovkin, V., Ciais, P., Fensholt, R., Tømmervik, H., Bala, G., Zhu, Z., Nemani, R. R., and Myneni, R. B.: China and India lead in greening of the world through land-use management, Nat Sustain, 2, 122–129, https://doi.org/10.1038/s41893-019-0220-7, 2019.

Chen, J., Chen, J., Liao, A., Cao, X., Chen, L., Chen, X., He, C., Han, G., Peng, S., and Lu, M.: Global land cover mapping at 30 m resolution: A POK-based operational approach, 103, 7–27, https://doi.org/10.1016/j.isprsjprs.2014.09.002, 2015.

Chen, L. and Dirmeyer, P. A.: Adapting observationally based metrics of biogeophysical feedbacks from land cover/land use change to climate modeling, Environ. Res. Lett., 11, 034002, https://doi.org/10.1088/1748-9326/11/3/034002, 2016.

Chen, H., Zeng, Z., Wu, J., Peng, L., Lakshmi, V., Yang, H., and Liu, J.: Large Uncertainty on Forest Area Change in the Early 21st Century among Widely Used Global Land Cover Datasets, Remote Sensing, 12, 3502, https://doi.org/10.3390/rs12213502, 2020.

Cs, M., G, S., and Y, Z.: Afforestation and forests at the dryland edges: lessons learned and future outlooks. In: Chen J, Wan S, Henebry G, Qi J, Gutman G, Sun G, Kappas M (szerk.) Dryland East Asia: Land dynamics amid social and climate change. HEP Publishers, Beijing & Walter de Gruyter and Co. Berlin, 2013, 245–264, https://doi.org/10.13140/RG.2.1.4325.4487, 2013.

Duveiller, G., Hooker, J., and Cescatti, A.: The mark of vegetation change on Earth's surface energy balance, Nat Commun, 9, 679, https://doi.org/10.1038/s41467-017-02810-8, 2018.

Duveiller, G., Caporaso, L., Abad-Viñas, R., Perugini, L., Grassi, G., Arneth, A., and Cescatti, A.: Local biophysical effects of land use and land cover change: towards an assessment

767   tool   for   policy   makers,   Land   Use   Policy,   91,   104382,

768   https://doi.org/10.1016/j.landusepol.2019.104382, 2020.

769 Fang, J., Guo, Z., Hu, H., Kato, T., Muraoka, H., and Son, Y.: Forest biomass carbon sinks in

770   East Asia, with special reference to the relative contributions of forest expansion and

771   forest   growth,   Global   Change   Biology,   20,   2019–2030,

772   https://doi.org/10.1111/gcb.12512, 2014.

773 Ge, J., Guo, W., Pitman, A. J., De Kauwe, M. G., Chen, X., and Fu, C.: The Nonradiative Effect

774   Dominates Local Surface Temperature Change Caused by Afforestation in China, 32,

775   4445–4471, https://doi.org/10.1175/JCLI-D-18-0772.1, 2019.

776 Hansen, M. C., Potapov, P. V., Moore, R., Hancher, M., Turubanova, S. A., Tyukavina, A.,

777   Thau, D., Stehman, S. V., Goetz, S. J., and Loveland, T. R.: High-resolution global maps

778   of   21st-century   forest   cover   change,   342,   850–853,

779   https://doi.org/10.1126/science.1244693, 2013.

780 Huang, L., Zhai, J., Liu, J., and Sun, C.: The moderating or amplifying biophysical effects of

781   afforestation on CO_2-induced cooling depend on the local background climate regimes

782   in   China,   Agricultural   and   Forest   Meteorology,   260–261,   193–203,

783   https://doi.org/10.1016/j.agrformet.2018.05.020, 2018.

784 Jia, G., Shevliakova, E., Artaxo, P., Noblet-Ducoudré, N. D., Houghton, R., Anderegg, W.,

785   Bastos, A., Bernsten, T. K., Cai, P., Calvin, K., Klein, C. D., Humpenöder, F., Kanter,

786   D., McDermid, S., Peñuelas, J., Pradhan, P., Quesada, B., Roe, S., Bernier, P., Espinoza,

787   J. C., Semenov, S., and Xu, X.: Climate Change and Land: an IPCC Special Report on

788   Climate Change, Desertification, Land Degradation, Sustainable Land Management,

789   Food Security, and Greenhouse Gas Fluxes in Terrestrial Ecosystems. 2019.

790 Juang, J.-Y., Katul, G., Siqueira, M., Stoy, P., and Novick, K.: Separating the effects of albedo

791   from eco-physiological changes on surface temperature along a successional

chronosequence in the southeastern United States, Geophys. Res. Lett., 34, 21, https://doi.org/10.1029/2007GL031296, 2007.

Kato, S., Rose, F. G., Rutan, D. A., Thorsen, T. J., Loeb, N. G., Doelling, D. R., Huang, X., Smith, W. L., Su, W., and Ham, S.-H.: Surface Irradiances of Edition 4.0 Clouds and the Earth's Radiant Energy System (CERES) Energy Balanced and Filled (EBAF) Data Product, 31, 4501–4527, https://doi.org/10.1175/JCLI-D-17-0523.1, 2018.

Lee, X., Goulden, M. L., Hollinger, D. Y., Barr, A., Black, T. A., Bohrer, G., Bracho, R., Drake, B., Goldstein, A., Gu, L., Katul, G., Kolb, T., Law, B. E., Margolis, H., Meyers, T., Monson, R., Munger, W., Oren, R., Paw U, K. T., Richardson, A. D., Schmid, H. P., Staebler, R., Wofsy, S., and Zhao, L.: Observed increase in local cooling effect of deforestation at higher latitudes, Nature, 479, 384–387, https://doi.org/10.1038/nature10588, 2011.

Lee, S. and Lee, D. K.: What is the proper way to apply the multiple comparison test?, Korean J Anesthesiol, 71, 353–360, https://doi.org/10.4097/kja.d.18.00242, 2018.

Li, Y., Zhao, M., Motesharrei, S., Mu, Q., Kalnay, E., and Li, S.: Local cooling and warming effects of forests based on satellite observations, Nature Communications, 6, 6603, https://doi.org/10.1038/ncomms7603, 2015.

Li, Y., Zhao, M., Mildrexler, D. J., Motesharrei, S., Mu, Q., Kalnay, E., Zhao, F., Li, S., and Wang, K.: Potential and Actual impacts of deforestation and afforestation on land surface temperature: IMPACTS OF FOREST CHANGE ON TEMPERATURE, J. Geophys. Res. Atmos., 121, 14,372-14,386, https://doi.org/10.1002/2016JD024969, 2016a.

Li, Y., De Noblet-Ducoudré, N., Davin, E. L., Motesharrei, S., Zeng, N., Li, S., and Kalnay, E.: The role of spatial scale and background climate in the latitudinal temperature response to deforestation, Earth Syst. Dynam., 7, 167–181, https://doi.org/10.5194/esd-7-167-

817   2016, 2016b.

818 Li, Y., Piao, S., Chen, A., Ciais, P., and Li, L. Z. X.: Local and teleconnected temperature

819   effects of afforestation and vegetation greening in China, National Science Review, 7,

820   897–912, https://doi.org/10.1093/nsr/nwz132, 2020.

821 Liang, W., Fu, B., Wang, S., Zhang, W., Jin, Z., Feng, X., Yan, J., Liu, Y., and Zhou, S.:

822   Quantification of the ecosystem carrying capacity on China's Loess Plateau, Ecological

823   Indicators, 101, 192–202, https://doi.org/10.1016/j.ecolind.2019.01.020, 2019.

824 Liu, Y.: China's forest resource dynamics based on allometric scaling relationship between

825   forest area and total stocking volume, Afr. J. Agric. Res., 7,

826   https://doi.org/10.5897/AJAR12.216, 2012.

827 Liu, Z., Ballantyne, A. P., and Cooper, L. A.: Increases in Land Surface Temperature in

828   Response to Fire in Siberian Boreal Forests and Their Attribution to Biophysical

829   Processes, Geophys. Res. Lett., 45, 6485–6494, https://doi.org/10.1029/2018GL078283,

830   2018.

831 Oleson, K., Lawrence, D., Bonan, G., Drewniak, B., Huang, M., Koven, C., Levis, S., Li, F.,

832   Riley, W., Subin, Z., Swenson, S., Thornton, P., Bozbiyik, A., Fisher, R., Heald, C.,

833   Kluzek, E., Lamarque, J.-F., Lawrence, P., Leung, L., and Yang, Z.-L.: Technical

834   description of version 4.5 of the Community Land Model (CLM),

835   https://doi.org/10.5065/D6RR1W7M, 2013.

836 Pan, Y., Birdsey, R. A., Fang, J., Houghton, R., Kauppi, P. E., Kurz, W. A., Phillips, O. L.,

837   Shvidenko, A., Lewis, S. L., Canadell, J. G., Ciais, P., Jackson, R. B., Pacala, S. W.,

838   McGuire, A. D., Piao, S., Rautiainen, A., Sitch, S., and Hayes, D.: A Large and

839   Persistent Carbon Sink in the World's Forests, 333, 988–993,

840   https://doi.org/10.1126/science.1201609, 2011.

841 Peng, S.-S., Piao, S., Zeng, Z., Ciais, P., Zhou, L., Li, L. Z. X., Myneni, R. B., Yin, Y., and

Zeng, H.: Afforestation in China cools local land surface temperature, Proceedings of the National Academy of Sciences, 111, 2915–2919, https://doi.org/10.1073/pnas.1315126111, 2014.Pongratz, J., Schwingshackl, C., Bultan, S., Obermeier, W., Havermann, F., and Guo, S.: Land Use Effects on Climate: Current State, Recent Progress, and Emerging Topics, Curr Clim Change Rep, 7, 99–120, https://doi.org/10.1007/s40641-021-00178-y, 2021.

Pitman, A. J., de Noblet-Ducoudré, N., Cruz, F. T., Davin, E. L., Bonan, G. B., Brovkin, V., Claussen, M., Delire, C., Ganzeveld, L., and Gayler, V.: Uncertainties in climate responses to past land cover change: First results from the LUCID intercomparison study, Geophys. Res. Lett., 36, https://doi.org/10.1029/2009GL039076, 2009.

Pitman, A. J., Avila, F. B., Abramowitz, G., Wang, Y. P., Phipps, S. J., and de Noblet-Ducoudré, N.: Importance of background climate in determining impact of land-cover change on regional climate, Nat. Clim. Chang., 1, 472–475, https://doi.org/10.1038/nclimate1294, 2011.

Qi, Y. and Wu, T.: The politics of climate change in China, WIREs Clim Change, 4, 301–313, https://doi.org/10.1002/wcc.221, 2013.

Shen, W., He, J., Huang, C., and Li, M.: Quantifying the Actual Impacts of Forest Cover Change on Surface Temperature in Guangdong, China, Remote Sensing, 12, 2354, https://doi.org/10.3390/rs12152354, 2020.

Sulla-Menashe, D. and Friedl, M. A.: User guide to collection 6 MODIS land cover (MCD12Q1 and MCD12C1) product, 1–18, 2018.

Swann, A. L., Fung, I. Y., and Chiang, J. C.: Mid-latitude afforestation shifts general circulation and tropical precipitation, Proceedings of the National Academy of Sciences, 109, 712–716, https://doi.org/10.1073/pnas.1116706108, 2012.

UC Berkely. Spring 2008 - Stat C141/ Bioeng C141 - Statistics for Bioinformatics

Winckler, J., Reick, C. H., Bright, R. M., and Pongratz, J.: Importance of Surface Roughness for the Local Biogeophysical Effects of Deforestation, J. Geophys. Res. Atmos., 124, 8605–8618, https://doi.org/10.1029/2018JD030127, 2019a.

Winckler, J., Lejeune, Q., Reick, C. H., and Pongratz, J.: Nonlocal Effects Dominate the Global Mean Surface Temperature Response to the Biogeophysical Effects of Deforestation, Geophys. Res. Lett., 46, 745–755, https://doi.org/10.1029/2018GL080211, 2019b.

Windisch, M. G., Davin, E. L., and Seneviratne, S. I.: Prioritizing forestation based on biogeochemical and local biogeophysical impacts, Nat. Clim. Chang., 11, 867–871, https://doi.org/10.1038/s41558-021-01161-z, 2021.

Zeng, Z., Wang, D., Yang, L., Wu, J., Ziegler, A. D., Liu, M., Ciais, P., Searchinger, T. D., Yang, Z.-L., Chen, D., Chen, A., Li, L. Z. X., Piao, S., Taylor, D., Cai, X., Pan, M., Peng, L., Lin, P., Gower, D., Feng, Y., Zheng, C., Guan, K., Lian, X., Wang, T., Wang, L., Jeong, S.-J., Wei, Z., Sheffield, J., Caylor, K., and Wood, E. F.: Deforestation-induced warming over tropical mountain regions regulated by elevation, Nature Geoscience, 14, 23–29, https://doi.org/10.1038/s41561-020-00666-0, 2021.

Zhang, L., Marron, J. S., Shen, H., and Zhu, Z.: Singular Value Decomposition and Its Visualization, Journal of Computational and Graphical Statistics, 16, 833–854, https://doi.org/10.1198/106186007X256080, 2007.

Zhang, Y., Chen, Y., Li, J., and Chen, X.: A Simple Method for Converting 1-km Resolution Daily Clear-Sky LST into Real LST, Remote Sensing, 12, 1641, https://doi.org/10.3390/rs12101641, 2020.

Zhao, K. and Jackson, R. B.: Biophysical forcings of land-use changes from potential forestry activities in North America, Ecological Monographs, 84, 329–353, https://doi.org/10.1890/12-1705.1, 2014.

Zhang, Z., Zhang, F., Wang, L., Lin, A., and Zhao, L.: Biophysical climate impact of forests

892   with different age classes in mid- and high-latitude North America, Forest Ecology and

893   Management, 494, 119327, https://doi.org/10.1016/j.foreco.2021.119327, 2021.

894